

**INSAT-3D and INSAT-3DR VIS and SWIR channel performance
monitoring through top-of-the-radiance over Desert and Ocean
target**

19/11/2019

Calibration and Validation Division
Earth, Ocean, Atmosphere, Planetary Sciences & Applications Area
Space Applications Centre (ISRO)
Ahmedabad – 380 015

Document control sheet

1	Report No.	SAC/EPESA/CVD/Cal-Val/11/19
2	Publication Date	November, 2019
3	Title	INSAT-3D and INSAT-3DR VIS and SWIR channel performance monitoring through top-of-the-radiance over Desert and Ocean target
4	Type of report	Scientific
5	Number of pages	30
6	Authors	K. N. Babu, Nandkishor
7	Originating unit	CVD/EPESA
8	Abstract	The radiometric calibration of a satellite sensor is the critical factor that ensures the success of satellite mission through the usefulness of the acquired data for quantitative applications. We describe here the time series analysis of top-of-the-atmosphere radiance measurements from INSAT-3D and -3DR visible and SWIR channel over desert and ocean target. This analysis gives the temporal stability/performance of sensor over these two reflectance target. The time series plot and scatter plot are suggesting that INSAT-3D visible channel TOA radiance is under performing with a bias of $\sim 30 \text{ W/m}^2/\text{sr}/\mu\text{m}$ as compared to INSAT-3DR over the land target and for the ocean target the bias is $\sim 6 \text{ W/m}^2/\text{sr}/\mu\text{m}$. The SWIR channel of INSAT-3D is showing slight over performance with bias of $\sim 1 \text{ W/m}^2/\text{sr}/\mu\text{m}$ in case of land target and negligible bias of $\sim 0.3 \text{ W/m}^2/\text{sr}/\mu\text{m}$ for ocean target.
9	Key words	Radiance, bias, geo-physical product, natural target
10	Security classification	Unrestricted
11	Distribution statement	Among all concerned

Contents

Table of Contents

Abstract	6
Introduction	6
Data and methodology	9
Results and Discussion	9
Relative radiometric performance test sites	9
INSAT-3D visible and SWIR channel performance over land and ocean site	10
INSAT-3DR visible and SWIR channel performance over land and ocean site	17
INSAT-3D and INSAT-3DR inter-satellite sensor comparison over ocean and land target	25
Conclusions	30
Acknowledgement	31
References	31

List of Figures

Figure No.		Page no.
1	The region of interest for monitoring INSAT-3D and INSAT-3DR visible and SWIR channel performance	8
2a	Histogram in percentage for INSAT-3D visible TOA radiances over land site.	11
2b	Histogram in percentage for INSAT-3D visible TOA radiances over ocean site	12
3a	The time series of top-of-the-atmosphere radiance of INSAT-3D visible channel over Little Rann of Kuchchh	13
3b	The time series of top-of-the-atmosphere radiance of INSAT-3D VIS channel over ocean target	14
4a	Histogram in percentage for INSAT-3D SWIR TOA radiances over land site	15
4b	Histogram in percentage for INSAT-3D SWIR TOA radiances over ocean site	16
5	The time series of top-of-the-atmosphere radiance of INSAT-3D SWIR channel over land and ocean target	17
6a	Histogram in percentage for INSAT-3DR visible TOA radiances over land site	18
6b	Histogram in percentage for INSAT-3DR visible TOA radiances over ocean site	18
7a	Histogram in percentage for INSAT-3DR SWIR TOA radiances over land site	19
7b	Histogram in percentage for INSAT-3DR SWIR TOA radiances over ocean site	20
8	The time series of top-of-the-atmosphere radiance of INSAT-3DR visible channel	21
9	The time series of top-of-the-atmosphere radiance of INSAT-3DR SWIR channel	22
10	Time series comparison plot of top-of-the-atmosphere radiance of INSAT-3D & -3DR visible channel	23
11	Time series comparison plot of top-of-the-atmosphere radiance of INSAT-3D & -3DR SWIR channel	24
12	Inter comparison of visible channel top-of-the-atmosphere radiance observed over land target	26
13	Inter comparison of visible channel top-of-the-atmosphere radiance observed over ocean target	27
14	Inter comparison of SWIR channel top-of-the-atmosphere radiance observed over land target	28
15	Inter comparison of SWIR channel top-of-the-atmosphere radiance observed over ocean target	29

List of Tables

1	Specifications of INSAT-3D and -3DR imager channels	7
---	---	---

Abstract

The radiometric calibration of a satellite sensor is the critical factor that ensures the success of satellite mission through the usefulness of the acquired data for quantitative applications. We describe here the time series analysis of top-of-the-atmosphere radiance measurements from INSAT-3D and -3DR visible and SWIR channel over desert and ocean target. This analysis gives the temporal stability/performance of sensor over these two reflectance target. The results of comparative time series analysis of top-of-the atmospheric radiance between INSAT-3D and INSAT -3DR imager for VIS and SWIR band confirm the performance of INSAT -3D imager shown in Figs.10 &11. The TOA bias of VIS and SWIR band TOA reflectance over time will impact the calculation of surface reflectance and other INSAT-3D imager geo-physical products. The time series plot and scatter plot are suggesting that INSAT-3D visible channel TOA radiance is under performing with a bias of $\sim 30 \text{ W/m}^2/\text{sr}/\mu\text{m}$ as compared to INSAT-3DR over the land target and for the ocean target the bias is $\sim 6 \text{ W/m}^2/\text{sr}/\mu\text{m}$. The SWIR channel of INSAT-3D is showing slight over performance with bias of $\sim 1 \text{ W/m}^2/\text{sr}/\mu\text{m}$ in case of land target and negligible bias of $\sim 0.3 \text{ W/m}^2/\text{sr}/\mu\text{m}$ for ocean target.

Introduction

The advancement and popularity of satellite data usage for societal benefits not only requires the development of new and complex satellites but also to improve the quality of satellite sensors and their data products. Therefore, it has become more essential to continually upgrade the ability to provide calibration of sensors. Generally, calibration procedure includes first radiometric calibration prior to the launch (Bruegge et al. 1998) and later the on-board calibration (Bruegge et al. 1993), but in the absence of onboard calibration facility, a post-launch vicarious calibration exercise provides an aid to compensate the degradation of the satellite sensor (Rao 2001). Vicarious calibration provides a method for calibration of satellite sensors using reference and precise measurements of spectral reflectance from the ground instruments over a terrestrial calibration site. These calibration coefficients can be incorporated for the accurate characterisation of the conversion of digital counts to radiance values. Vicarious calibration is a broadly adopted technique for continuous monitoring the radiometric performance of satellite sensor, which involves the uncertainties computation in the calibration coefficients to correct the radiometric

response of the sensor (Thome et al. 1998). Vicarious calibration is performed with radiance simulation using measured ground reflectance and atmospheric parameters on clear day with less aerosol conditions to those at the satellite level.

The Indian National Satellite (INSAT)-3D/-3DR, developed by the Indian Space Research Organization (ISRO), were launched on 26th July 2013 and 8th September 2016, respectively. INSAT-3D and INSAT-3DR satellite series equipped with a 6-channels Imager and 19- channels atmospheric sounder, which operate in visible to thermal infrared region of the electromagnetic spectrum. Imager from both the satellites operate from a geostationary altitude 36000 km in visible (VIS) and shortwave infra-red (SWIR) bands with 1 km spatial resolution, while Mid-Wave Infra-Red (MWIR), Thermal Infra-Red-1 (TIR1), Thermal Infra-Red-2 (TIR2) and Water Vapor (WV) bands with 4 km spatial resolution respectively. However, sounder from INSAT-3D/-3DR has 18 infrared (IR) channels ranging from 3.7 to 14.7 μm and one visible channel for the daytime cloud detection with 10 km spatial resolution. The significant improvements incorporated in INSAT-3DR are: (1) Imaging in MWIR band to provide nighttime pictures of low clouds and fog and (2) Imaging in the split band TIR channel with two separate windows (10.2-11.2 and 11.5-12.5 μm regions) with 4 km spatial resolution provides estimation of sea surface temperature with better accuracy. Imager from both the satellites provide data at every 30 minutes interval with 15 minutes difference, which means that data sets are available at every 15 minutes intervals collectively. Details about wavelength range and spatial resolution of imager is given in Table-1.

Table 1: Specifications of INSAT-3D and -3DR imager channels

Band No.	Wavelength (μm)	Resolution (km)
1	VIS (0.55-0.75)	1
2	SWIR (1.55-1.70)	1
3	MWIR (3.8-4.0)	4
4	WV(6.5-7.1)	8
5	TIR-1 (10.2-11.3)	4
6	TIR-2 (11.5-12.5)	4

Monitoring the radiometric performance characteristics of sensor is an essential step in the estimation of reliable, continuous geo-physical products for quantitative applications. This radiometric calibration which converts the digital number to engineering units has been performed

in laboratory to acquire consistently accurate radiometric values over the sensor design life. To secure the radiometric calibration validity and the continuity of satellite data, pre- and post-launch calibration has been proposed to determine the characteristics of radiometric calibration. Because the pre-launch, lab calibration performance degrades due to severe environmental conditions encountered after launch, operational space-borne satellites need to be monitored to obtain their absolute radiometric characteristics during its operational time frame. For the in-orbit calibration, on-board, vicarious, lunar, and cross-calibration techniques have been suggested (Abdou, et. al., 2002; Kerola, et. al., 2009; Kamei, et. al., 2012; Liu, et. al., 2010; Seo, 2014; Thome, et. al., 2003).

This report envisaged the performance monitoring of INSAT-3D and -3DR visible and SWIR channels over the desert and ocean site through time series top-of-the-atmosphere radiance measurements of respective sensors. Also the vicarious calibration exercises using in-situ measurements over desert site of Little Rann of Kuchchh. The Figure 1 shows region of investigation, where the time series analysis is carried out at both places and the vicarious calibration is performed over land site only (red square).

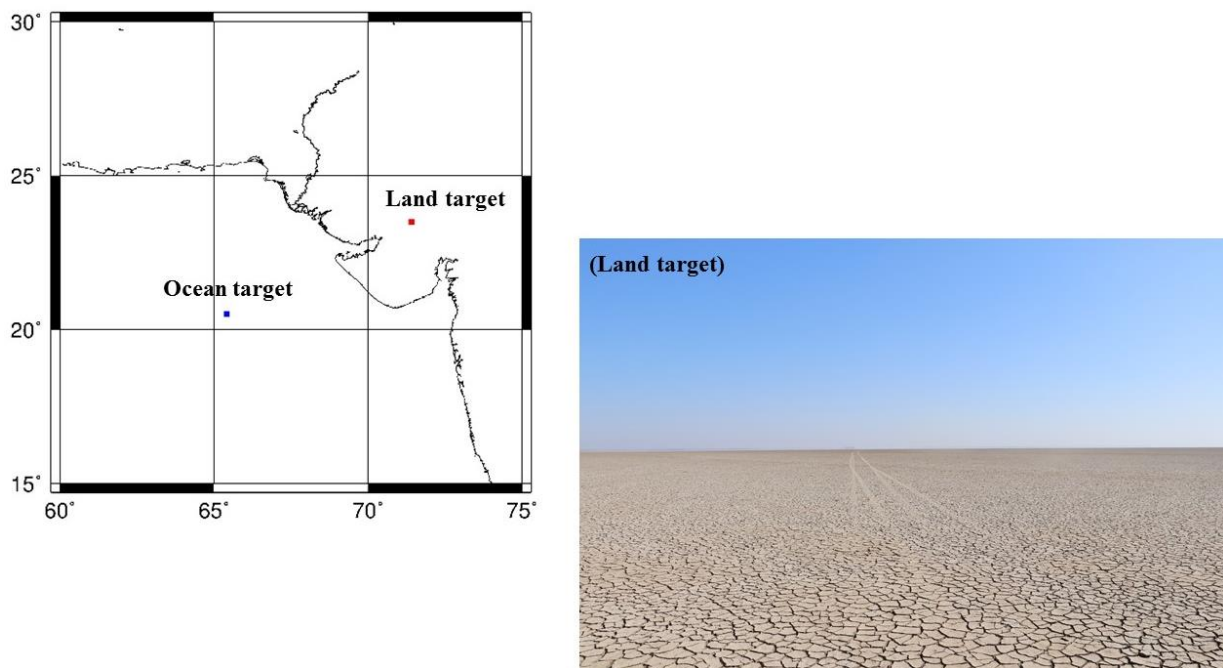


Figure 1: The region of interest for monitoring INSAT-3D and INSAT-3DR visible and SWIR channel performance.

Data and methodology

INSAT-3D/-3DR standard full disk Level 1B data product (SAC/IMDPS/IPA/DPSG/MSDPD/TN-01/FEB) has been used in the present study (www.mosdac.gov.in). INSAT-3D/-3DR measured brightness values received in terms of a digital number (DN) for each band are converted to TOA spectral radiance $L(\lambda)$ values either using the lookup table or using the calibration coefficients. The look up table (LUT) provides mapping from DN to corresponding radiance values. The LUT is generated using calibration coefficients, which are provided as a filed name “Radiometric Calibration Type” in the data product as attribute. Lab and online radiometric calibration coefficients are available as part of attribute in the data product, which can be used for computing radiance directly from DN. Lab coefficients are provided in terms of slope, offset and quadratic term in the provided product, which are generated using pre-launch ground test data. Whereas online calibration is performed using on-board internal blackbody serving as a hot target and space view count as cold target, which provides two online slope and offset values. Quadratic term is derived using inter sensor calibration. More details about the procedures for both the calibration coefficients are given in the INSAT-3D/-3DR data products format document, 2014 (SAC/IMDPS/IPA/DPSG/MSDPD/TN-01/FEB). While estimating the radiance values the DNs should be inverted, if a field name “invert”=true in the attribute indicates the image DNs are inverted. The coefficients provided for DN to radiance conversion are used as follows:

$$DN_{inv} = DN_{max} - DN \quad (\text{only if } invert = true) \quad (1)$$

Where DN_{inv} is the inverted DN value. $DN_{max} = 1023$ for imager.

$$L(\lambda) \text{ (in } mw \text{ cm}^{-2} \text{ sr}^{-1} \mu\text{m}^{-1}) = labonline_radiance_quad \cdot (DN)^2 + labonline_radiance_scale_factor \cdot DN \quad (2)$$

Here, DN is digital numbers recorded by the sensor. The values for the slope (scale factor), offset and quadratic term to convert DN to radiance for each band are provided in the attribute.

Results and Discussion

Relative radiometric performance test sites

Attributing to their preferable stability of surface characteristics and atmospheric dynamics, pseudo invariant sites are commonly used for monitoring the radiometric performance stability, degradation monitoring and inter-comparisons (Chander et al. 2010; Bouvet 2014) especially for

the satellite sensors without on-board calibration facilities. The Committee on Earth Observation Satellites (CEOS) Working group on Calibration and Validation identified several test sites around the world (Teillet and Chander, 2010) based on the selection criteria, such as low probability of atmospheric variability, high spatial homogeneity, weak directional effects, flat reflectivity spectrum. Based on these criteria, we have selected one desert sites in Little Rann of Kutch (LROK) and one ocean site in Arabian sea.

INSAT-3D visible and SWIR channel performance over land and ocean site

Desert site in Little Rann of Kutch (LROK), Gujarat with an altitude of ~6 m above mean sea level. This site is extended more than 60 km² area, presenting a completely flat and homogenous terrain characterized by high surface reflectance (Figure 1). The area is a vast, homogenous, plain land with mostly dry, salty soil dominating the landscape during the months of December to May, and prone to excessive water logging during the monsoon season (June – September). The site is a clay-dominated dry land with different spectral characteristics that have been used for radiometric calibration sites for large footprint sensors (e.g. INSAT-3A, INSAT-3D and INSAT-3DR). The field data collection campaigns are being conducted to perform the vicarious calibration of visible and SWIR channels of ISRO's optical sensors over this desert site and the same region is chosen to study the temporal stability performance interns of its measured radiance at the TOA level. The yearly histogram of TOA in percentage for INSAT-3D is given in Figure 2.

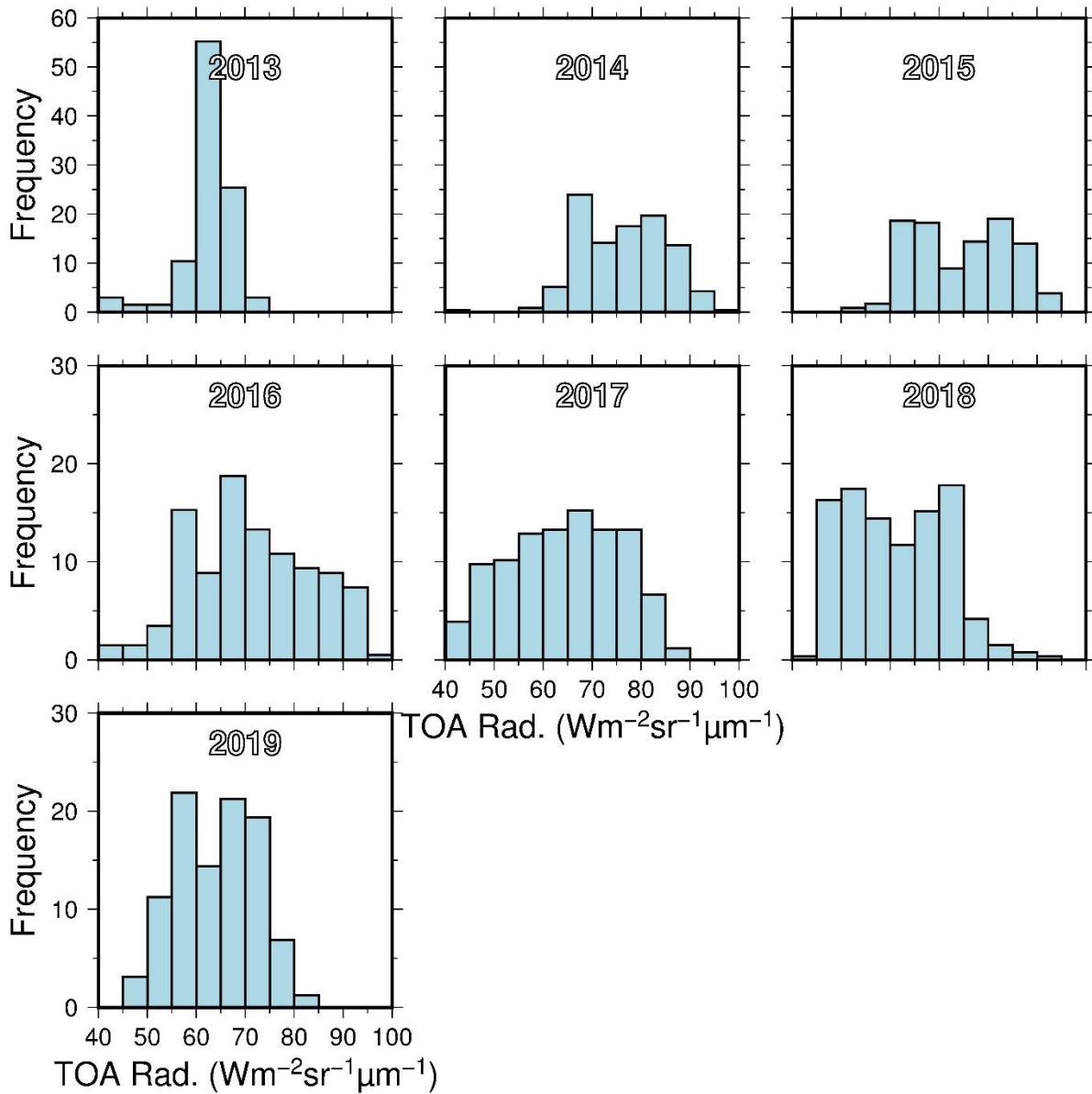


Figure 2a: Histogram in percentage for INSAT-3D visible TOA radiances over land site.

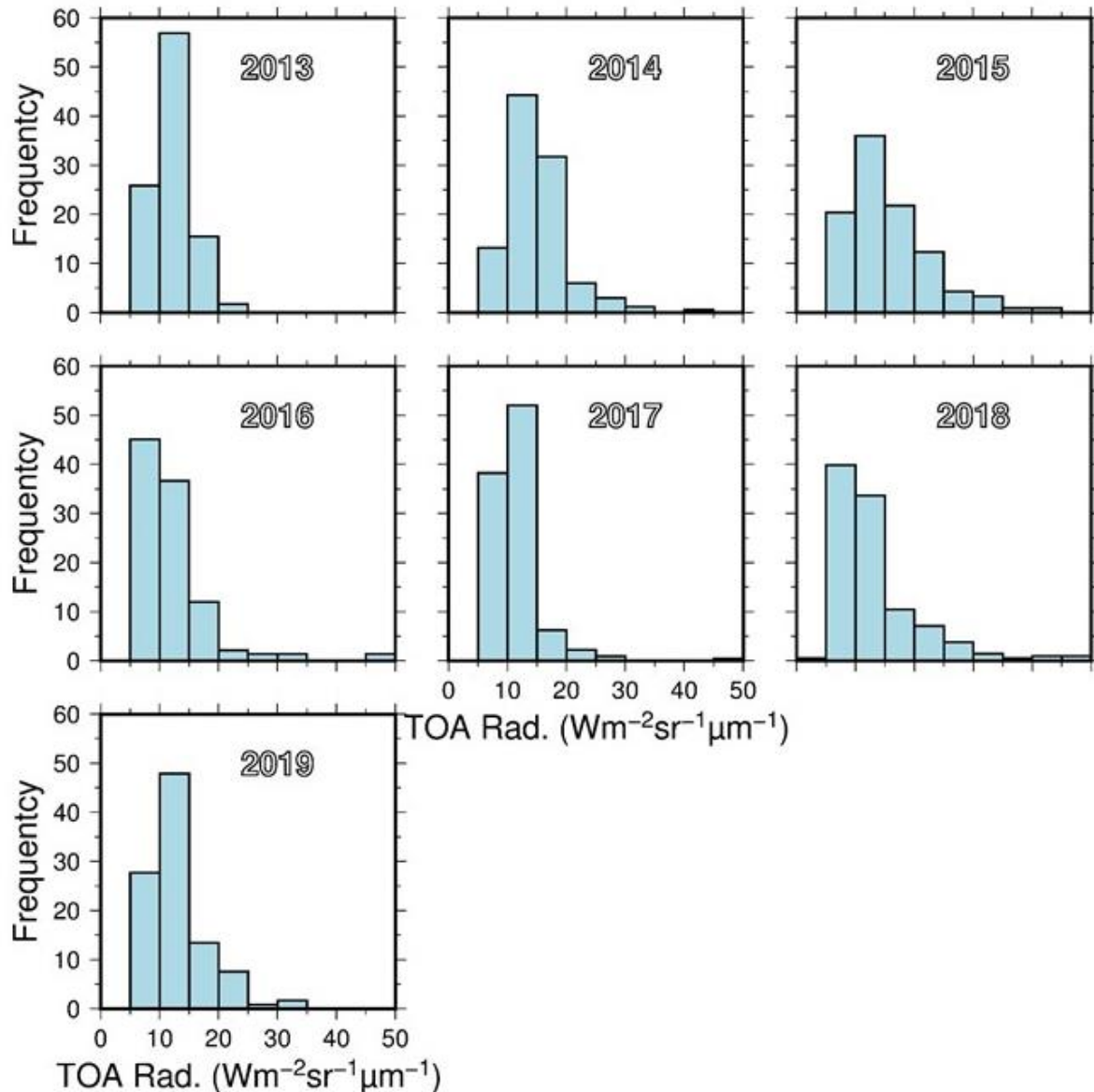


Figure 2b: Histogram in percentage for INSAT-3D visible TOA radiances over ocean site.

A single averaged value over 7 x 7 pixels which are corresponding at 7:00GMT are considered for one day and other observations are not considered for the analysis. The histogram statistics are computed from mean value lies within 10% of coefficient of variance using all grid pixel points (7x7 grid). From the figure we can observe that 90% of the TOA mean values are spread between 60 and 85 W/m²/sr/μm over the land target upto the year 2016 with very less contribution from lower TOA radiances. However, beyond 2016 the significant spread is observed at the lower scale. A similar histogram trend is noticed in case of visible channel TOA radiance over the ocean site

(Figure 2b). The nature of spread gives very clear indication about INSAT-3D performance in terms of TOA radiance over the ocean site than compare to desert site.

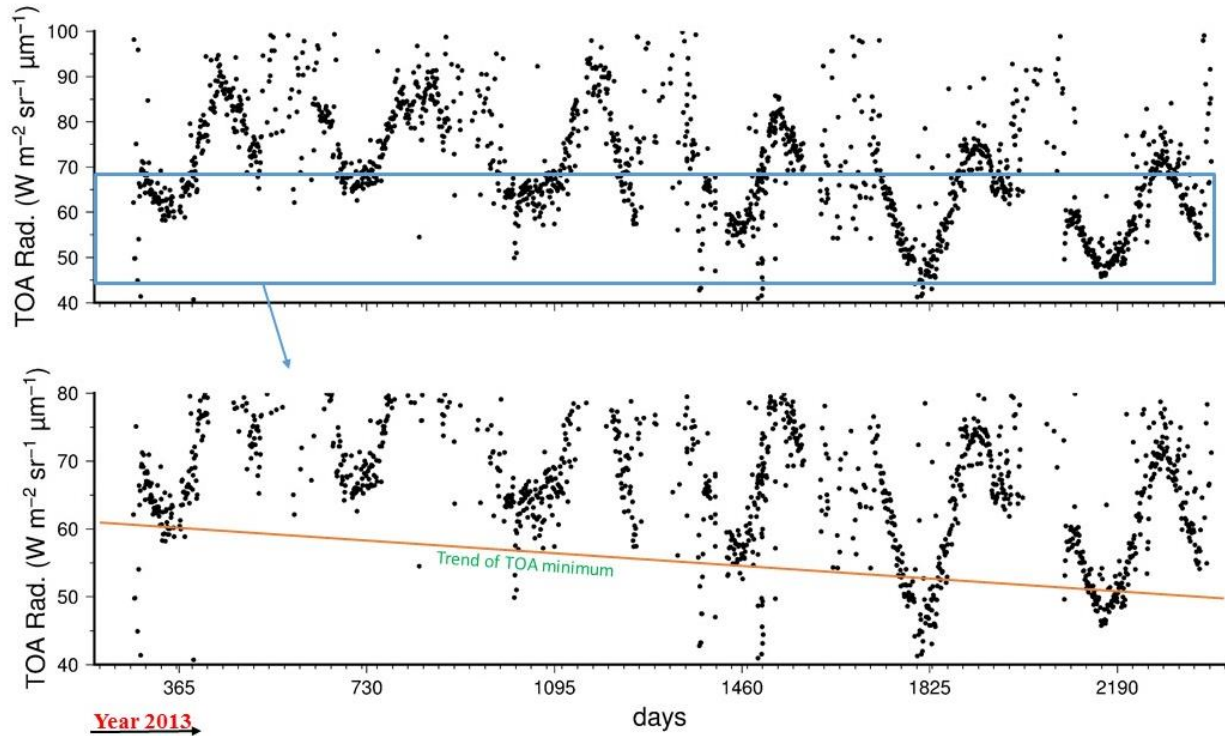


Figure 3a: The time series of top-of-the-atmosphere radiance of INSAT-3D visible channel over Little Rann of Kuchchh.

The TOA radiance time series over the land site and ocean site is shown in Figure 3. Each dot represents the mean value of 7x7 pixels of visible channel TOA radiance. Figure shows that majority of points shows clear trend of INSAT-3D performance with small scatter, the scatter points are due to low visibility of terrestrial target owing to clouds or presence of dust events at the time of satellite sensor scanning. Neglecting such points/events, the general performance trend indicates a significant change (decrease) in TOA radiance of visible channel from the year 2016 and declining trend beyond the year 2016. The trend over ocean target shows systematic pattern each year with lowest TOA radiance during winter season. The reflectivity of land target changes year to year and the atmosphere over land changes very fast as compared to ocean, hence we can see overall TOA radiance pattern shift. Seeing the performance over both targets conclusive inference can be noticed: the performance of INSAT-3D visible channel is repetitive till the year

2016 and decreasing latter. The amount of decrease need to be calculated vicariously using the land target measurements and atmospheric measurements synchronous with the satellite sensor scan.

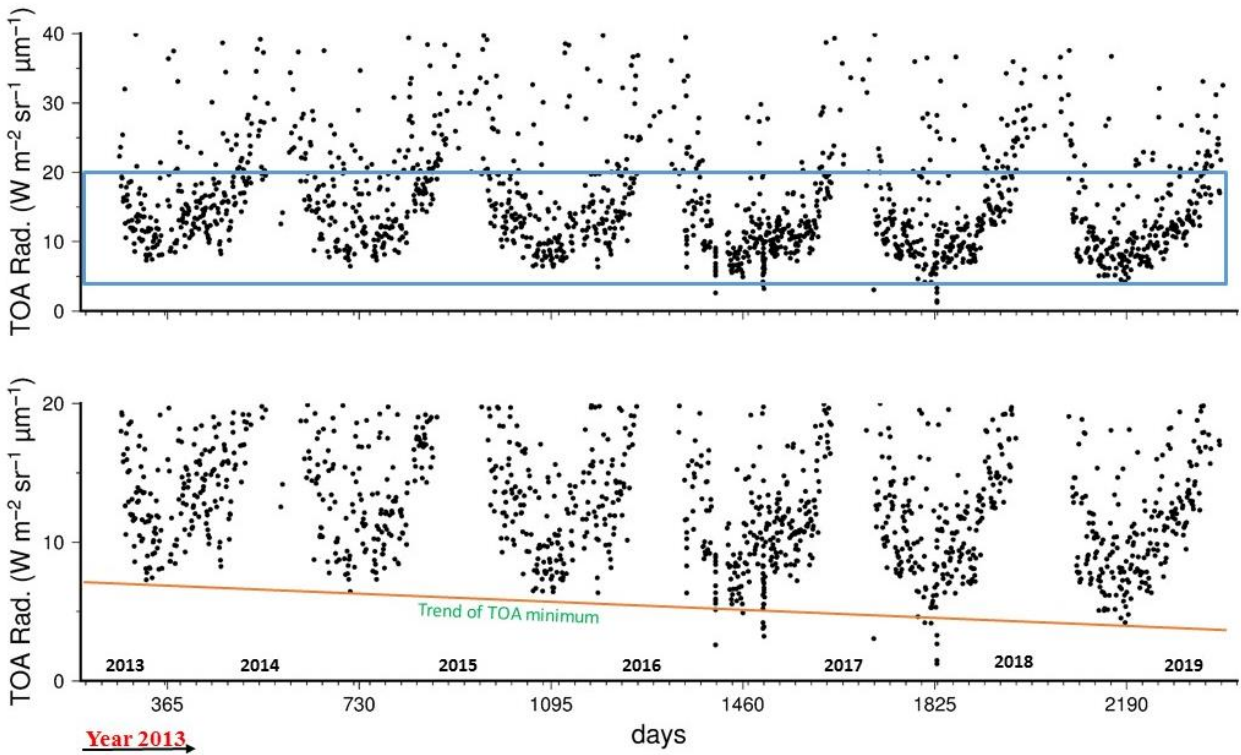


Figure 3b: The time series of top-of-the-atmosphere radiance of INSAT-3D VIS channel over ocean target.

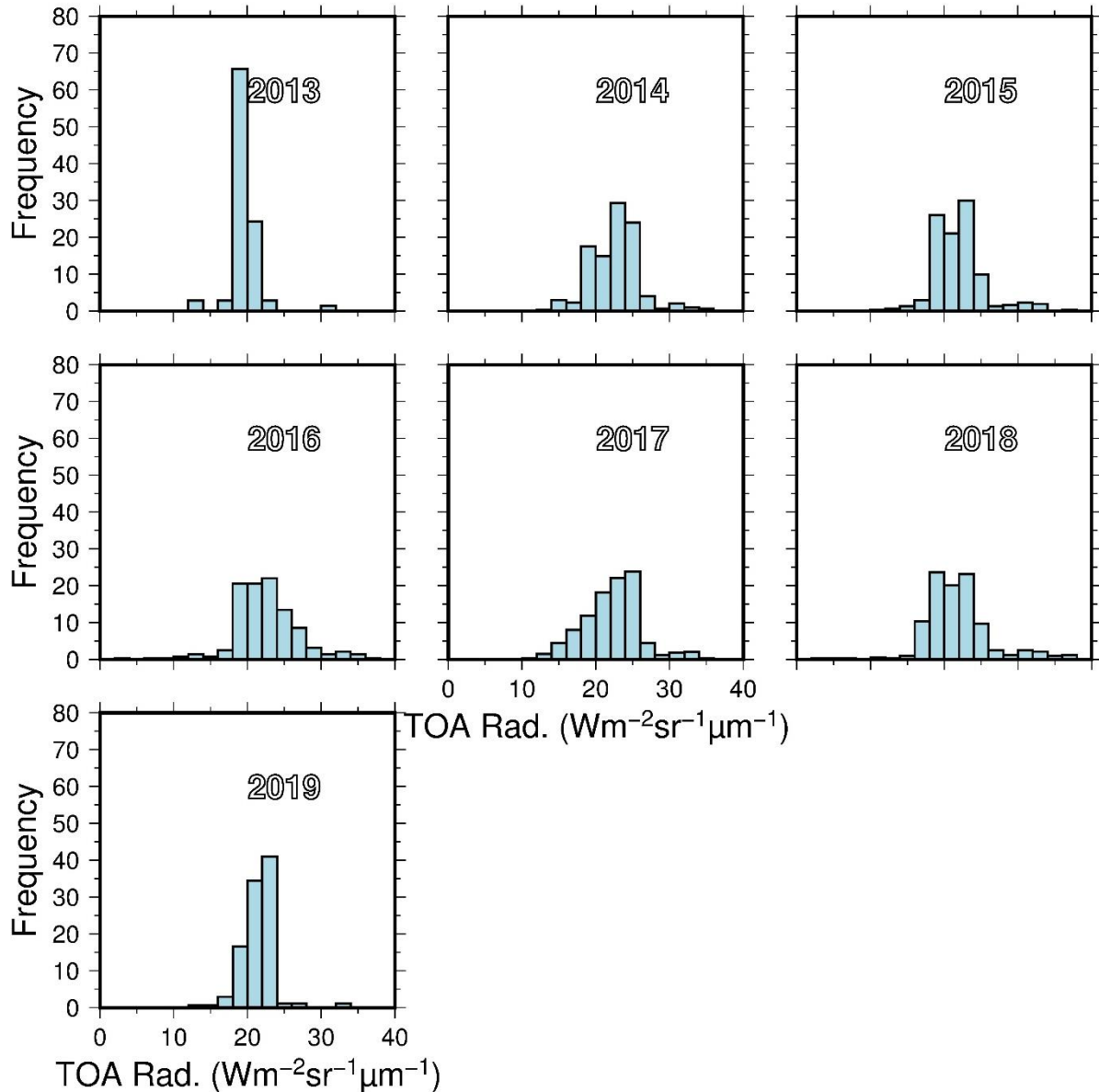


Figure 4a: Histogram in percentage for INSAT-3D SWIR TOA radiances over land site.

The histogram plot for INSAT-3D SWIR channel TOA radiance is shown in Figure 4. The data set for histogram plot are prepared similar to the visible channel. From the figure we can observe that 90% of the TOA mean values are spread between 18 and 24 W/m²/sr/μm over the land target upto the year 2016 with very less contribution from lower TOA radiances. However, beyond 2016 the significant spread is observed at the higher scale. A similar histogram trend is noticed in case of SWIR channel TOA radiance over the ocean site (Figure 4b).

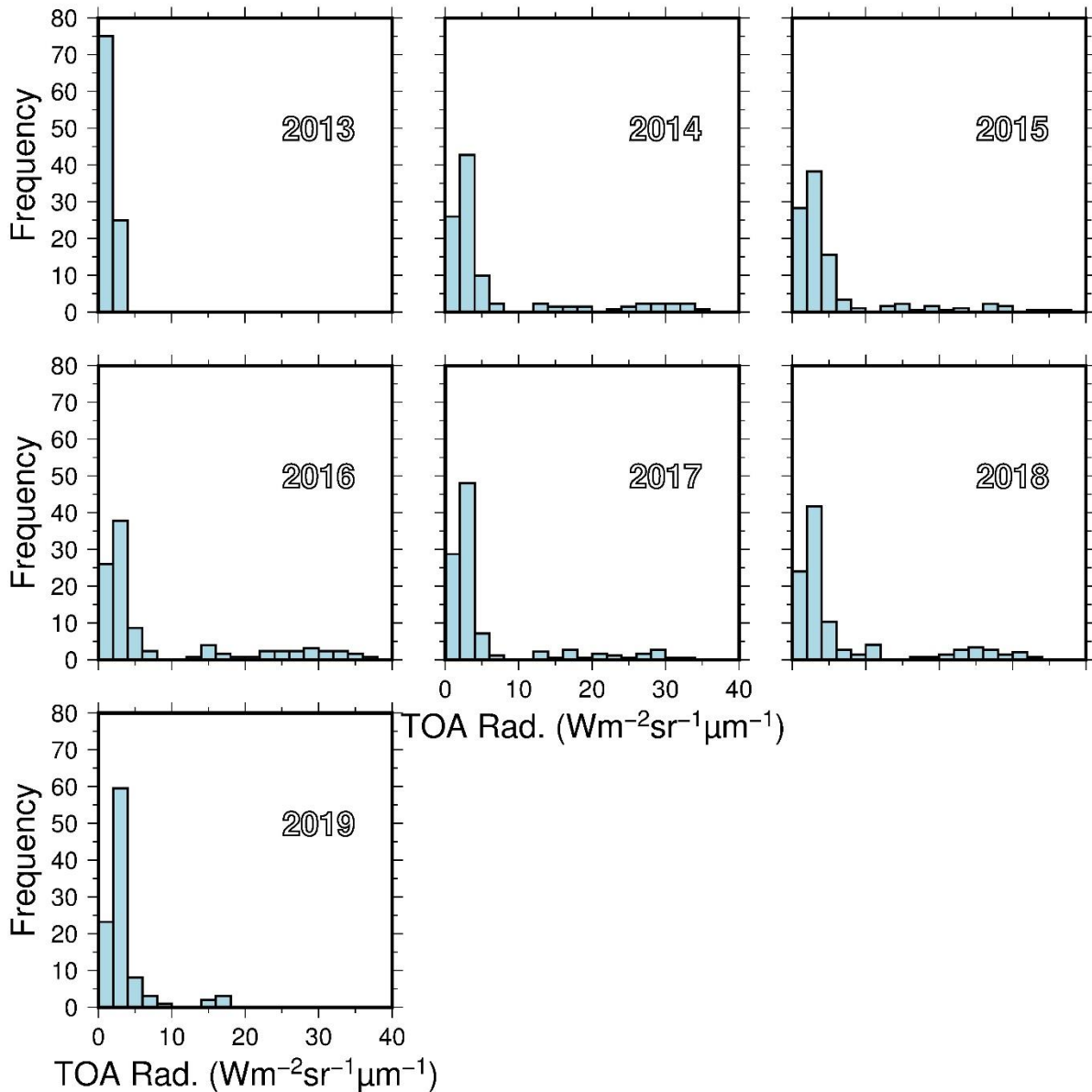


Figure 4b: Histogram in percentage for INSAT-3D SWIR TOA radiances over ocean site.

The TOA radiance time series over the land target and ocean target is shown in Figure 5. Each dot represents the mean value of 7x7 pixels of SWIR channel TOA radiance. Figure shows that majority of points shows clear trend of INSAT-3D performance with small scatter, unlike visible channel TOA radiance the scatter of points are less which may be due to low visibility of terrestrial target owing to clouds or presence of dust events at the time of satellite sensor scanning. Neglecting such points/events, the general performance trend indicates a slight increase in TOA radiance of

SWIR channel from the year 2016. The trend over ocean target shows systematic pattern each year with lowest TOA radiance during winter season.

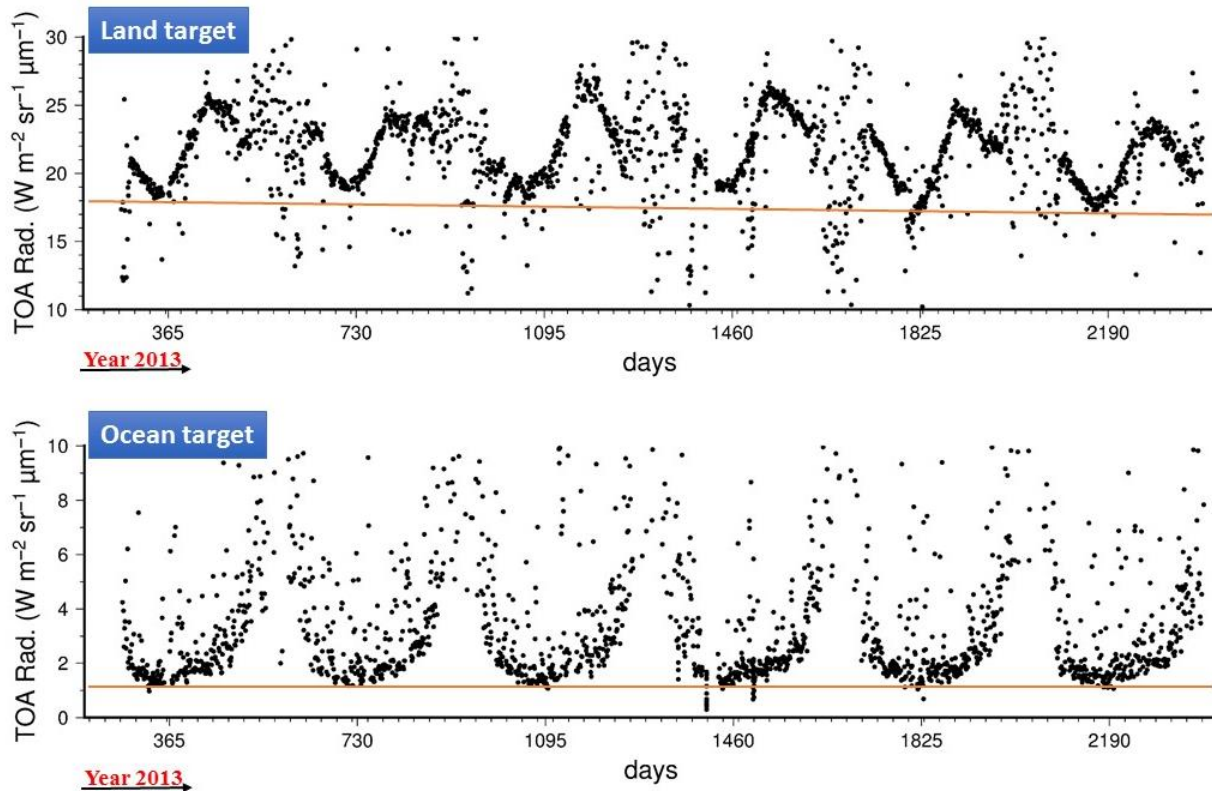


Figure 5: The time series of top-of-the-atmosphere radiance of INSAT-3D SWIR channel over land and ocean target.

INSAT-3DR visible and SWIR channel performance over land and ocean site

The histogram plot for INSAT-3DR visible channel TOA radiance is shown in Figure 6. The 90% of the TOA radiance mean values are spread between 70 and 105 $W/m^2/sr/\mu m$ over the land target with similar trend since the year 2016. A similar histogram trend is noticed in case of SWIR channel TOA radiance over the ocean site (Figure 4b). The nature of spread gives very clear indication about INSAT-3D performance in terms of TOA radiance over the ocean site than compare to desert site.

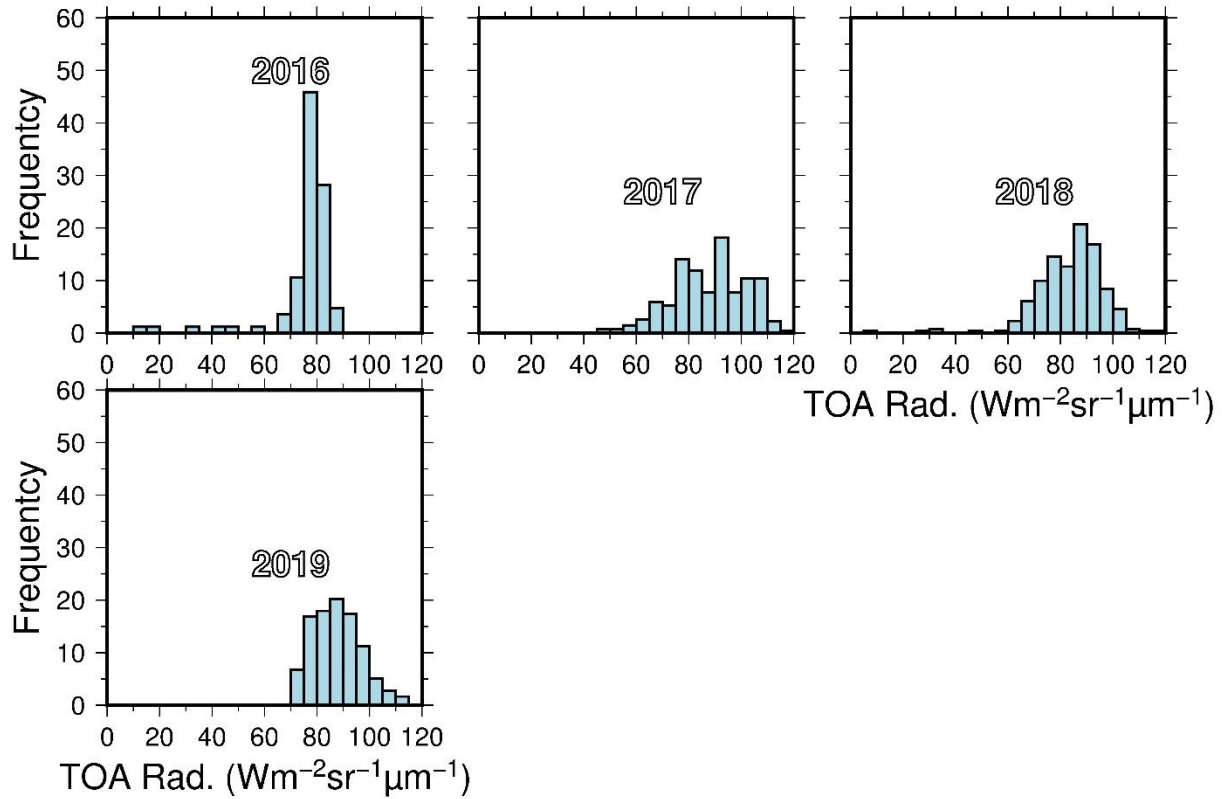


Figure 6a: Histogram in percentage for INSAT-3DR visible TOA radiances over land site.

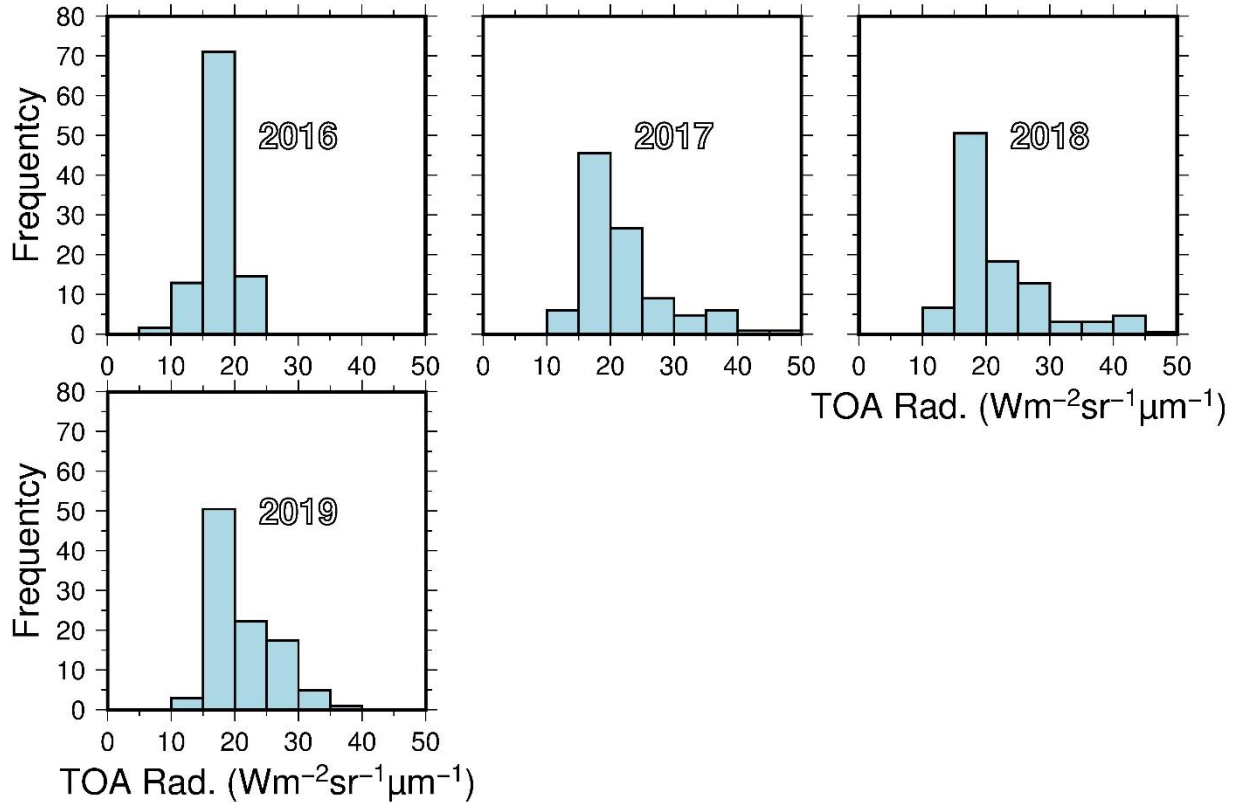


Figure 6b: Histogram in percentage for INSAT-3DR visible TOA radiances over ocean site.

The histogram plot for INSAT-3DR SWIR channel TOA radiance is shown in Figure 7. It is observed the most of the TOA radiance mean values are spread between 15 and 20 $W/m^2/sr/\mu m$ over the land target in the year 2016. After 2016 the mean values of TOA radiance are observed with slightly spread between 15 and 25 $W/m^2/sr/\mu m$ over the land target up to 2019. These results indicate that these little changes may be caused due to variation in soil moisture resulting from meteorological conditions.

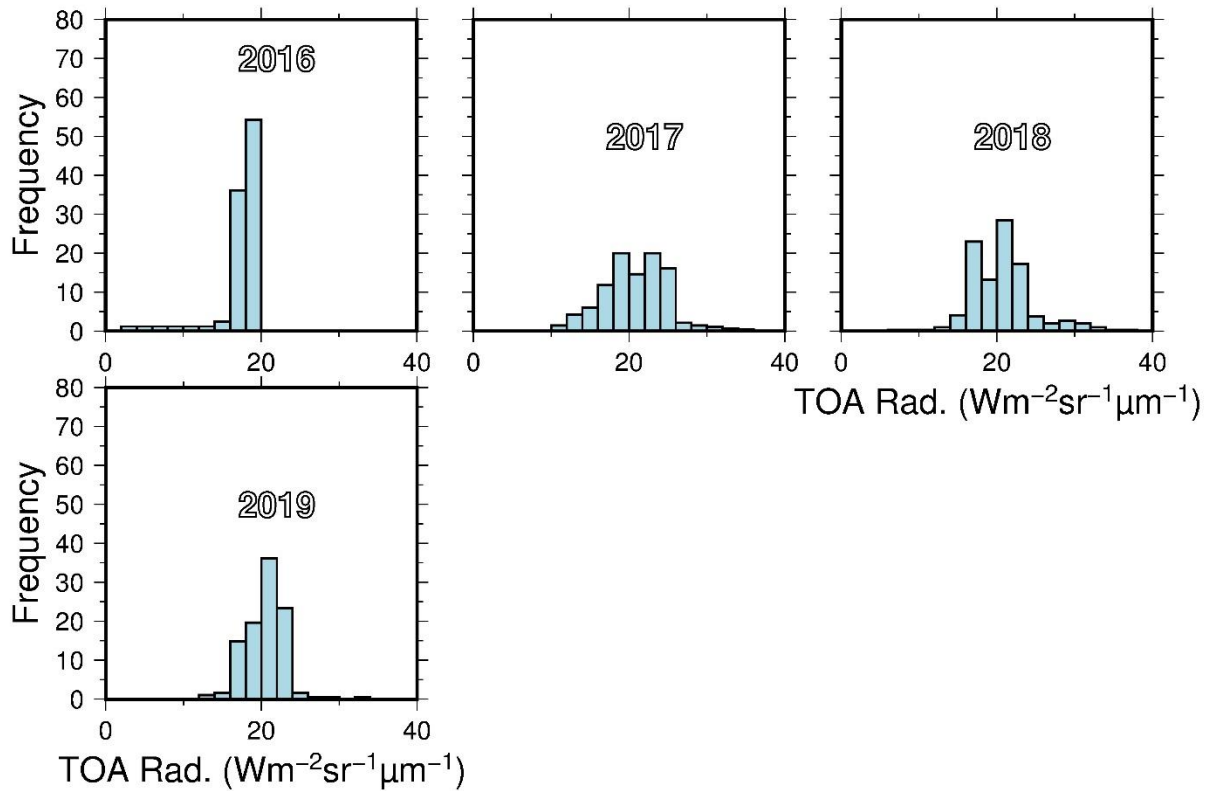


Figure 7a: Histogram in percentage for INSAT-3DR SWIR TOA radiances over land site.

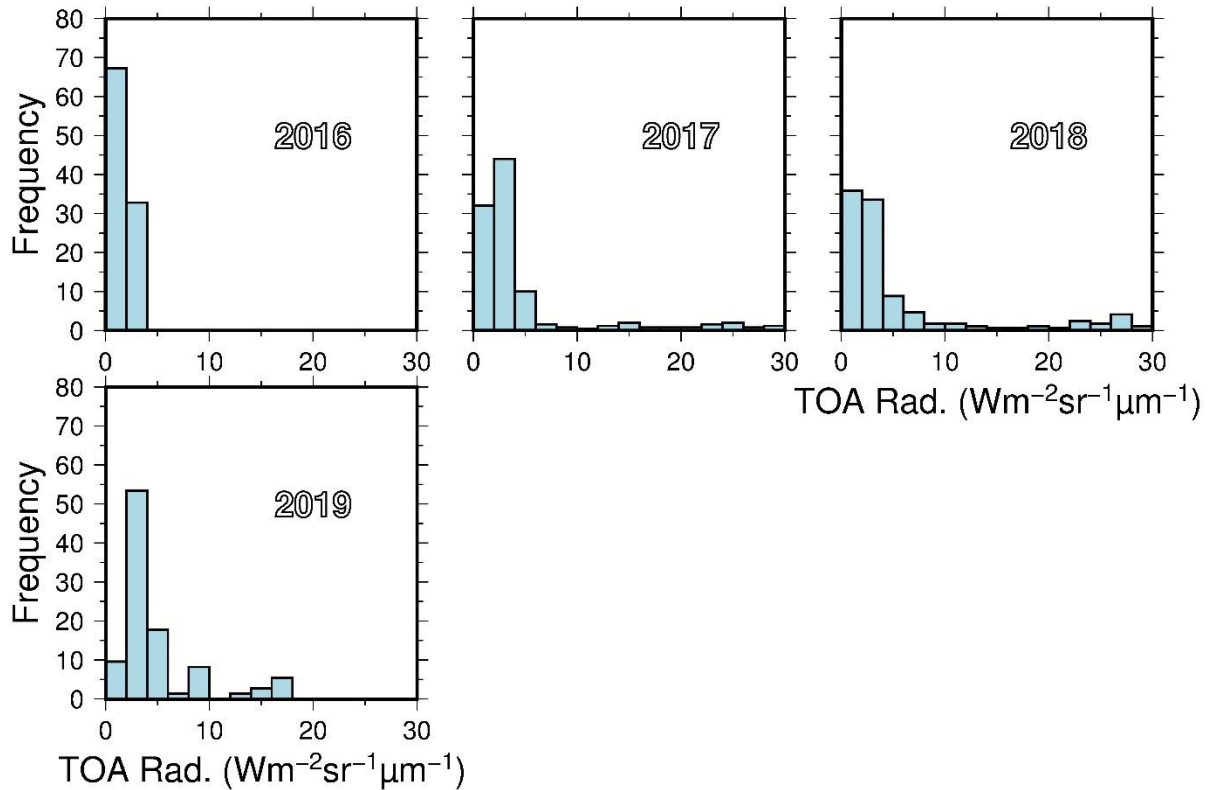


Figure 7b: Histogram in percentage for INSAT-3DR SWIR TOA radiances over ocean site.

The histogram for INSAT-3DR SWIR channel TOA radiance over ocean site is shown in Figure 7b. The SWIR channel TOA radiance values are lower than visible channel because of water has relatively low reflectance in SWIR channel, with clear water having the greatest reflectance in the blue portion of the visible part of the spectrum and Turbid water has a higher reflectance in the visible region than clear water. Water has high absorption and virtually no reflectance in near infrared wavelengths range and beyond. Ice and snow generally have high reflectance across all visible wavelengths. Reflectance decreases in the near infrared portion and there is very low reflectance in the SWIR region. The low reflection of ice and snow in the SWIR is related to their microscopic liquid water content. Reflectance differs for snow and ice depending on the actual composition of the material including impurities and grain size.

The time series of top-of-the-atmosphere radiance of INSAT-3DR visible channel over land and ocean is shown in figure 8. In Figure 8 over the ocean and land target we are drawn a reference line which shows that the TOA radiance value has a certain lower radiance value in winter season .and shows

that similar pattern in rest of the year. The time series plot clearly shows the performance of INSAT- 3DR visible channel over the Ocean target with similar pattern from the year 2016. But over the land target there is some data points have low TOA radiance value below a certain reference level and it indicates that this little change may be due to some dust storm or may be due to some other atmospheric conditions during that time. The higher values of TOA radiance are observed due to higher reflection from clouds. The SWIR channel also shows similar pattern over land and ocean target with less radiance value comparative to visible channel (Figure 9). Over all we can say there is no major changes in performance of INSAT-3DR Visible and SWIR channel from year 2016.

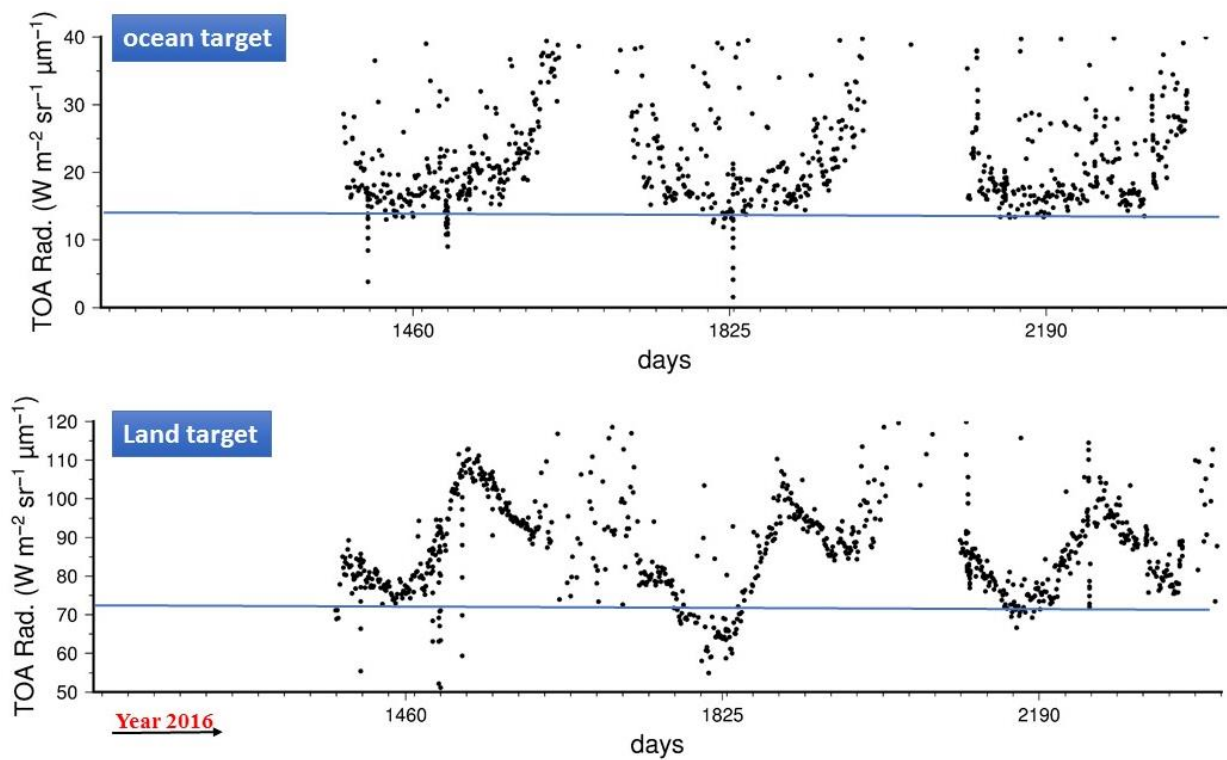


Figure 8: The time series of top-of-the-atmosphere radiance of INSAT-3DR visible channel.

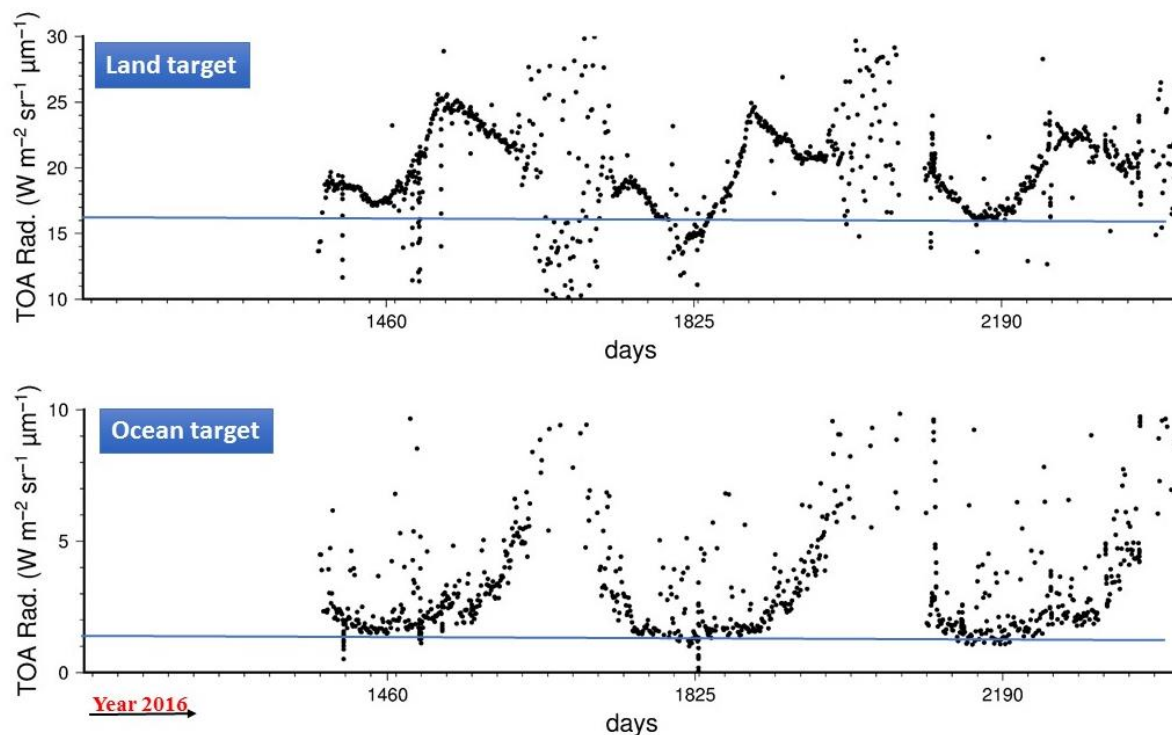


Figure 9: The time series of top-of-the-atmosphere radiance of INSAT-3DR SWIR channel.

In Figure 10, the time series plot between INSAT-3D and 3DR visible channel over the land and ocean target are shown. The black and red dots are representing the average radiance value of 7x7 pixel over the land and ocean targets for INSAT-3D and -3DR respectively. The time series plot over the land target between INSAT-3D & -3DR clearly shows that INSAT-3DR imager captured more radiance value than the INSAT-3D. Figure 10 describes the comparison of the TOA radiance measured by INSAT-3D and INSAT-3DR imager over the land and ocean target for each day at 7:00GMT with average radiance value of 7x7 pixel over both the targets. This study aims towards the assessment of the performance of both imager channels with less uncertainty in the reflectance measurement is due to significant variation in the surface characteristics over the region. Although the choice of the site was guided by the research already reported in the literature on the post launch calibration of geostationary satellite imagery, according that radiometric stability of the calibration site implies long-term stability of the TOA albedo (and of seasonal variation, if any) or reflectance over large spatially uniform area. Another feature is to have high surface reflectance

to maximize the signal-to-noise ratio and minimize atmospheric effects on the radiation measured by the satellite. In addition, low incidence of clouds would enhance the usefulness of the site.

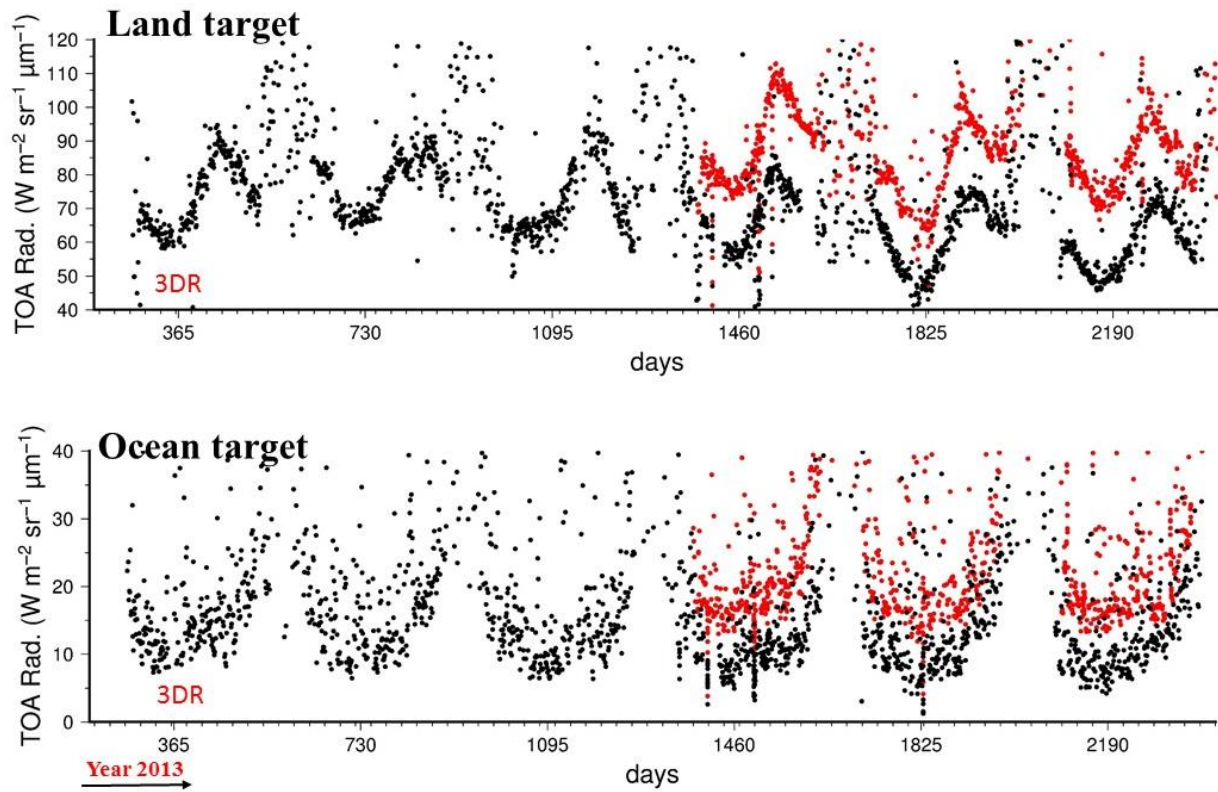


Figure 10: Time series comparison plot of top-of-the-atmosphere radiance of INSAT-3D & -3DR visible channel.

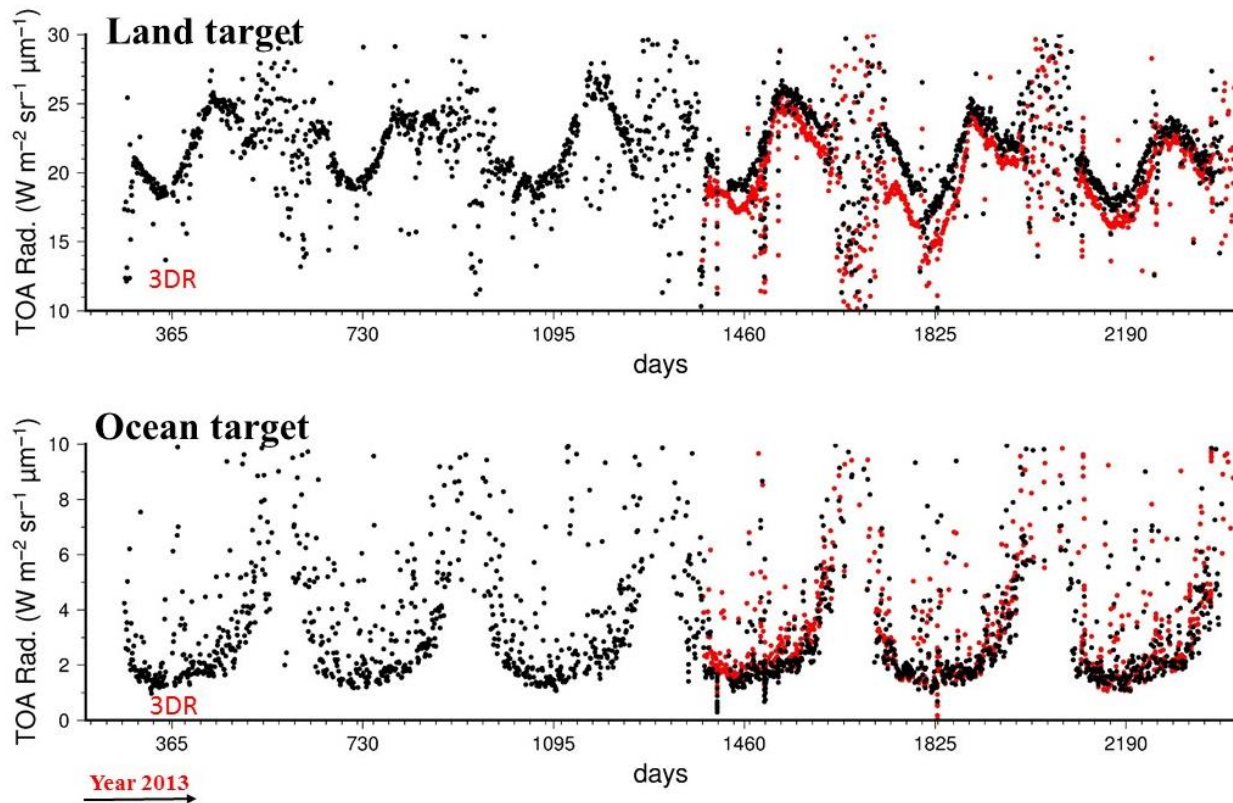


Figure 11: Time series comparison plot of top-of-the-atmosphere radiance of INSAT-3D & -3DR SWIR channel.

Figure 11, describe the time series comparison of top of the atmospheric radiance of SWIR channel over the ocean and land site for INSAT-3D and -3DR with black and red dots respectively. The measured TOA radiance for the desert site and the ocean site plotted as a time series to determine the trend of the in-orbit performance of the INSAT-3D and -3DR imager. The most noticeable feature is a gradual decrease in measured radiance for visible channel of INSAT-3D as can be seen in the results shown in Figure10. It also should be noted that the measured TOA radiance in SWIR channel of INSAT-3DR imager have less radiance value comparatively INSAT-3D imager over desert site. The seasonal changes occur in measured TOA radiance which can be easily seen in Fig. 11, Over the land target the TOA radiance value abnormally varies from trending pattern during each year may be caused of cloud contamination and due to rain or may be due to dust storm for visible channel and also for SWIR channel. However, the ocean target yield significantly different trend of TOA radiance also abnormally changed in each year during a certain time period may be caused of bright clouds or may be due to other atmospheric conditions. But it is observed that over the ocean target the time series plot for both INSAT-3D and -3DR imager have similar

trend with very significant difference in measured TOA radiance value for SWIR channel. While in visible channel over the ocean target the TOA radiance value measured by INSAT-3D and -3DR imager have high difference comparative to SWIR channel.

INSAT-3D and INSAT-3DR inter-satellite sensor comparison over ocean and land target

The TOA radiance comparisons of visible channel of INSAT-3D and -3DR over the targets of land and ocean are shown in figures 12 and 13 respectively. The comparisons are done for the years 2016 to 2019 over the target sites as shown in figure 1. The visible channel of 3DR TOA radiance average minimum value over land target remains at $\sim 65 \text{W/m}^2/\text{sr}/\mu\text{m}$ while 3D remains close to $45 \text{W/m}^2/\text{sr}/\mu\text{m}$. An insignificant numbers of data points of higher values beyond $95 \text{W/m}^2/\text{sr}/\mu\text{m}$ are found in both INSAT-3D and -3DR visible channel over the land target and they are removed for the statistics as their occurrences are less which means they may not be a true signature of the target. Data editing on matched data points are not performed since logical reasons could not be arrived in this work. Slope of the best linear fit for the four years are stable between 0.7 and 0.8 with adjusted R^2 between ~ 0.7 and ~ 0.8 . The time series plot and scatter plot are suggesting that INSAT-3D visible channel TOA radiance is under performing with a bias of $\sim 30 \text{W/m}^2/\text{sr}/\mu\text{m}$ as compared to INSAT-3DR over the land target. The bias values are relative and the absolute value can be estimated vicariously through radiative transfer simulations.

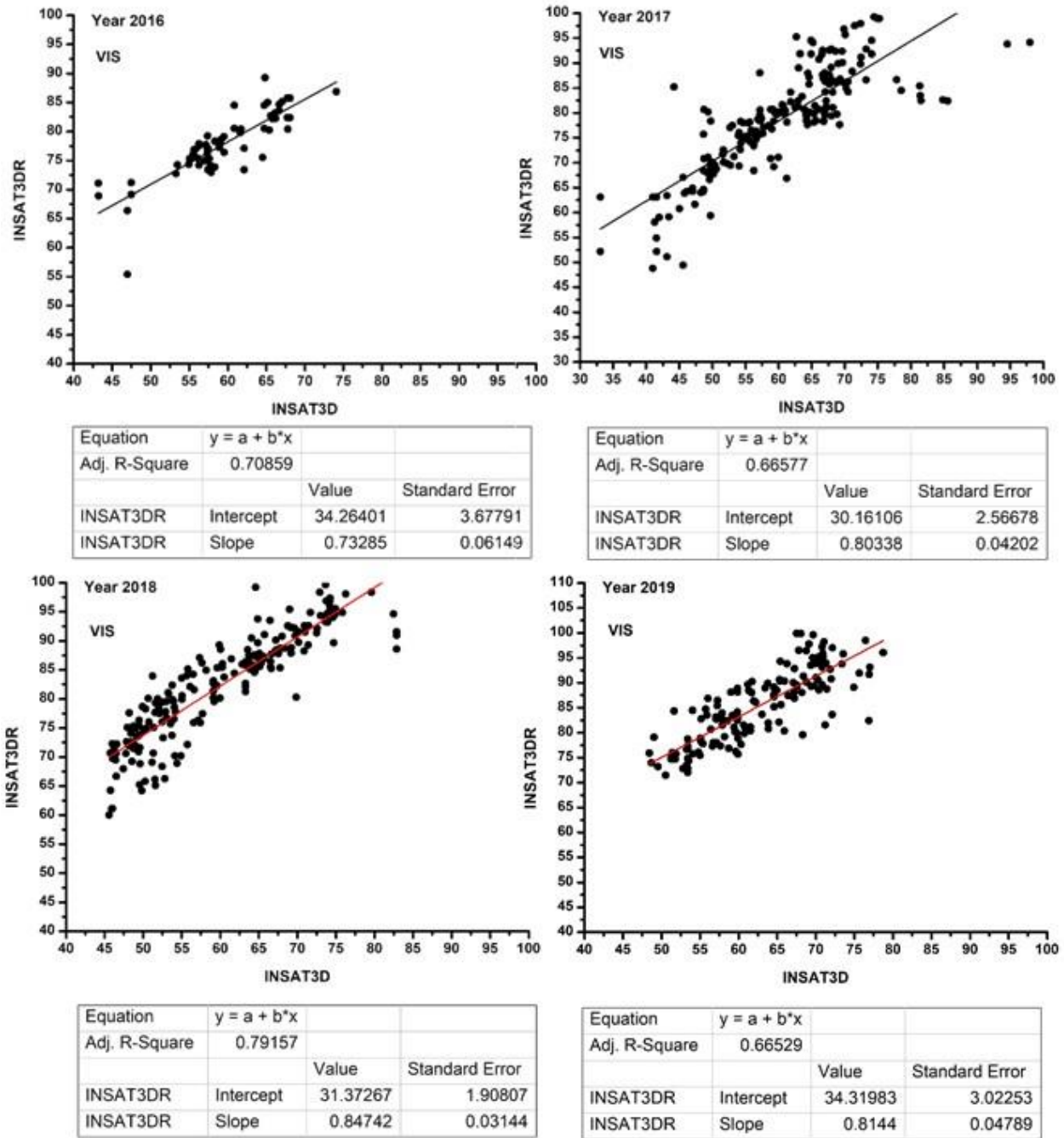


Figure 12: Inter comparison of visible channel top-of-the-atmosphere radiance observed over land target.

The scatter plots between INSAT-3D and -3DR measured TOA radiance describes the correlation for VIS channel over the land target in figure 12. The maximum correlation of $R^2=0.79$ is observed during the year 2018 with slope value 0.84 and minimal value (0.03) of standard error over the land target. It is also found

that the slope is increasing with time and standard error decreasing with time during 2016 to 2018. But in the year 2019 the slope is slightly decreased and the standard error is increased.

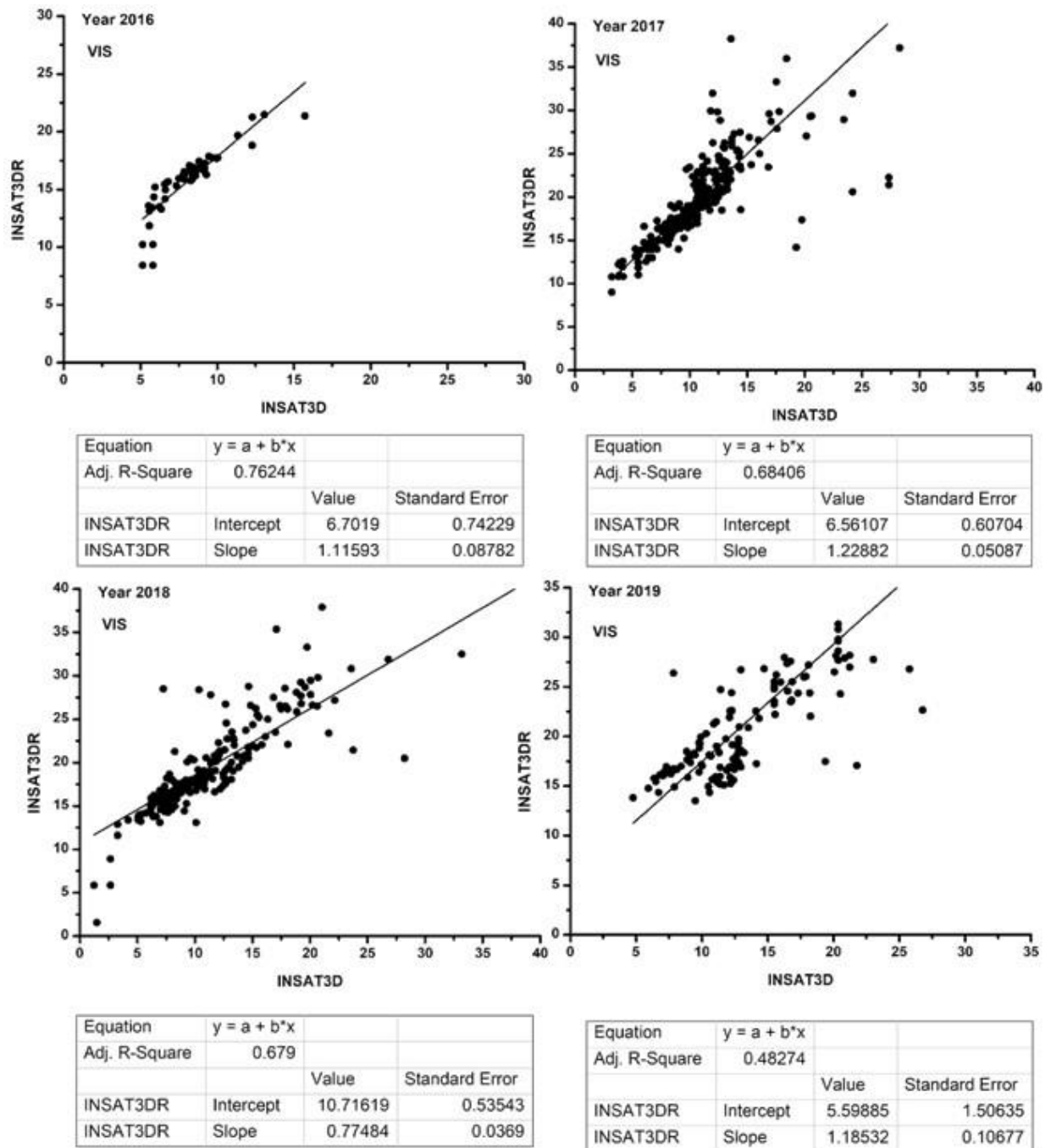


Figure 13: Inter comparison of visible channel top-of-the-atmosphere radiance observed over ocean target.

Figure 13 describes the year wise scatter plots between INSAT-3D and INSAT-3DR imager derived TOA radiance for the VIS channel over the ocean target from 2016 to 2019. The acceptable statistical agreement

has been observed between INSAT-3D and 3DR derived radiance along with adjusted $R^2=0.68$ and the standard error is found to be minimal (~ 0.03) during 2018. It is observed that the correlation factor decrease and the standard error increase with time and it is found minimum during 2019. The correlation between INSAT-3D and 3DR derived radiance is found to be less over the ocean target than land target.

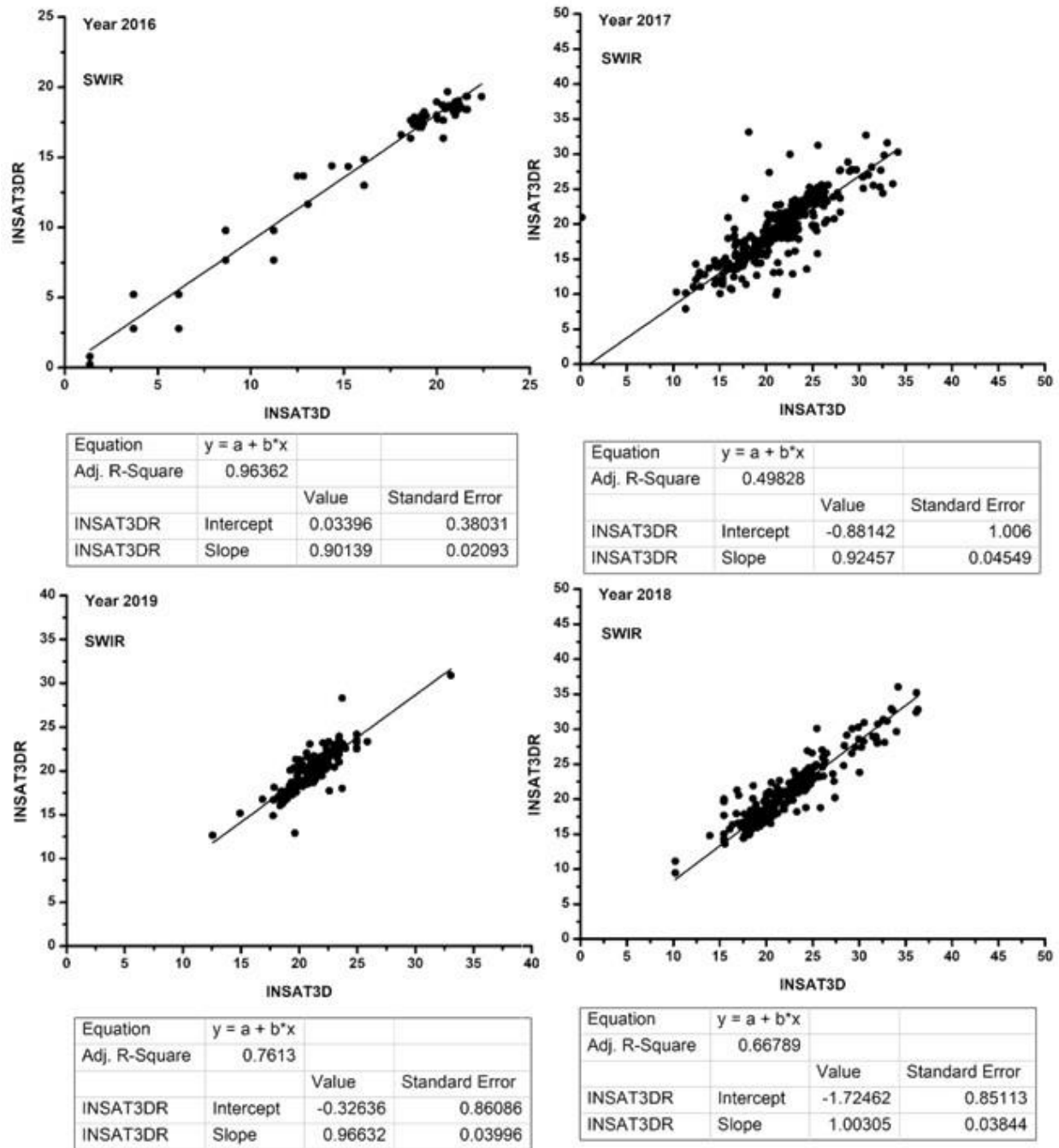


Figure 14: Inter comparison of SWIR channel top-of-the-atmosphere radiance observed over land target

Similarly, the results of combined linear regression for SWIR channel between INSAT-3D and -3DR over the target of land and ocean is shown in figure 14 and figure 15 respectively. Figure 14 describes the

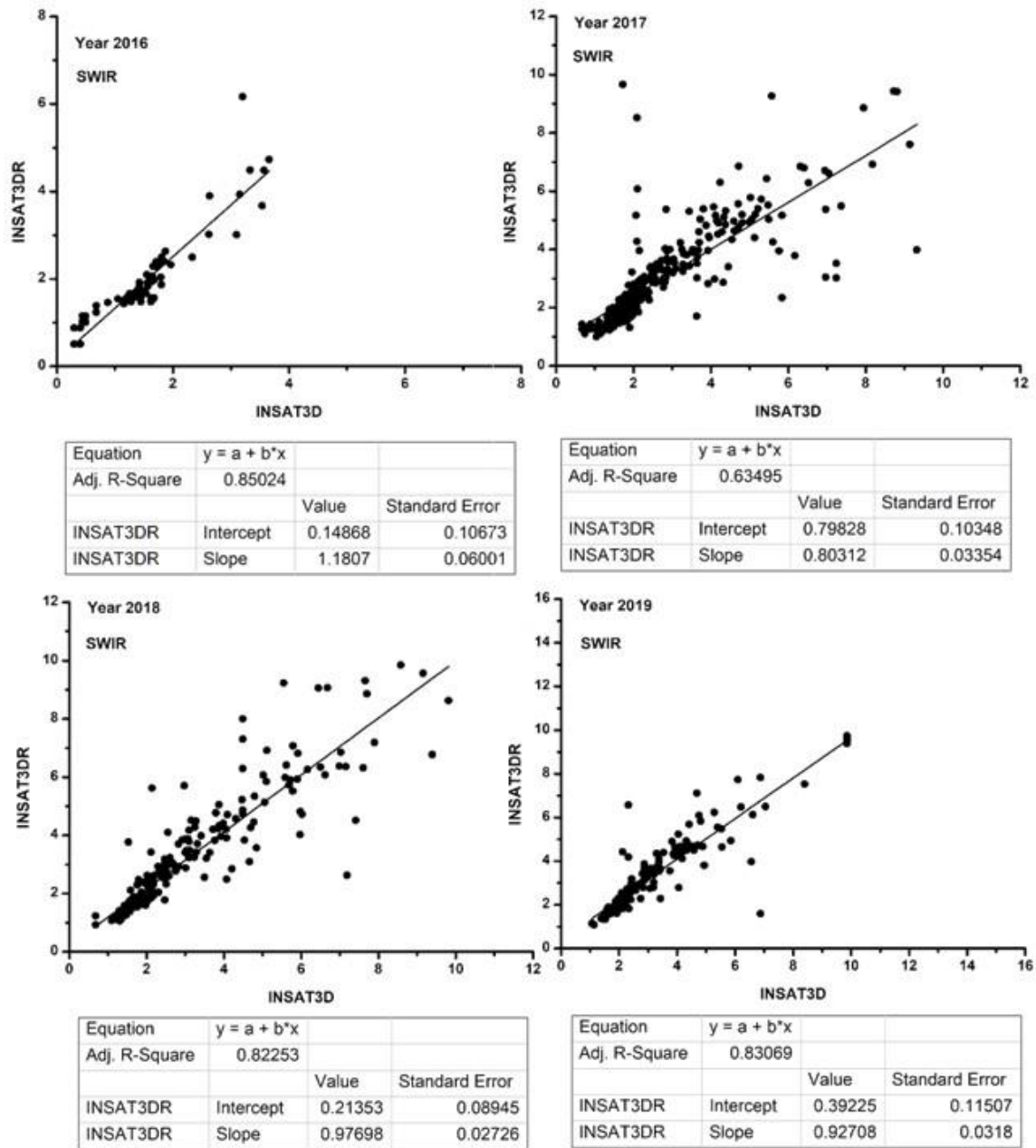


Figure 15: Inter comparison of SWIR channel top-of-the-atmosphere radiance observed over ocean target.

correlation between INSAT-3D and -3DR derived TOA radiance for SWIR channel over the land target. It is observed that for SWIR channel the correlation between -3D and -3DR radiance have good statistical agreement with $R^2 = 0.96$ and standard error is found to be minimal (0.02) over

the land target in 2016. In year 2017, the correlation value is observed to 0.49 and the standard error is found to be 0.04. The results describe that the correlation value increase and the standard error decrease with time and the slope also remain stable during the time and has minimal value (0.90) with relative error of 0.02 in year 2016.

Figure 15 describes the scatter plots between INSAT-3D and -3DR imager derived TOA radiance of SWIR channel over the ocean target. Good statistical agreement has been observed between INSAT-3D and -3DR derived TOA radiance with $R^2=0.8$ and standard error between 0.03 to 0.06 during 2016 to 2019. The scatter plots for SWIR channel also shows the correlation between both satellite measured TOA radiance over the ocean target is more than the land target during 2018, 2019, with the value of 0.83 and 0.82 respectively. The standard error is also found to be very less comparative to land target with 0.03 and 0.02 during the year 2018 and 2019 respectively. But in year 2016 and 2017 the correlation between INSAT-3D and INSAT-3DR observed TOA radiance is less over the ocean target than land target.

Conclusions

Analysis shows that the degradation of the INSAT-3D imager resulted the TOA radiance observed by imager gradually decrease from the trend observed by INSAT-3D imager with greater impact in VIS (0.55-0.75 μm) band over the land and ocean targets shown in Fig.3. The results of comparative time series analysis of top-of-the atmospheric radiance between INSAT-3D and INSAT -3DR imager for VIS and SWIR band confirm the performance of INSAT -3D imager shown in Figs.10 &11. The TOA bias of VIS and SWIR band TOA reflectance over time will impact the calculation of surface reflectance and other INSAT-3D imager geo-physical products. The time series plot and scatter plot are suggesting that INSAT-3D visible channel TOA radiance is under performing with a bias of $\sim 30\text{W}/\text{m}^2/\text{sr}/\mu\text{m}$ as compared to INSAT-3DR over the land target and for the ocean target the bias is $\sim 6\text{W}/\text{m}^2/\text{sr}/\mu\text{m}$. The SWIR channel of INSAT-3D is showing over performance with bias of $\sim 1\text{W}/\text{m}^2/\text{sr}/\mu\text{m}$ in case of land target and negligible bias of $\sim 0.3\text{W}/\text{m}^2/\text{sr}/\mu\text{m}$ for ocean target.

Acknowledgement

The authors gratefully acknowledge the encouragement received from Director, SAC for carrying out the present research work. Valuable suggestions received from Deputy Director, EPSA are also gratefully acknowledged. Authors are also thankful to the Cal-Val team member for their supports.

References

1. Abdou, W. A., et. al., 2002. "Vicarious calibration experiment in support of the multi-angle imaging spectroradiometer," *IEEE Trans. Geosci. Remote Sens.*, 40, 1500–1511.
2. Bruegge, C. J., Duval, V. G., Chrien, N. L., Korechoff, R. P., Gaitley, B. J., & Hochberg, E. B. (1998). MISR prelaunch instrument calibration and characterization results. *IEEE Transactions on Geoscience and Remote Sensing*, 36, 1186–1198.
3. Bruegge, C. J., Stiegman, A. E., Rainen, R. A., & Springsteen, A. W. (1993). Use of Spectralon as a diffuse reflectance standard for inflight calibration of earth-orbiting sensors. *Optical Engineering*, 32, 805–814.
4. Bouvet, M., 2014. Radiometric comparison of multispectral imagers over a pseudo-invariant calibration site using a reference radiometric model. *Remote Sens. Environ.* 140, 141–154.
5. Chander, G., Xiong, X., Choi, T., Angal, A., 2010. Monitoring on-orbit calibration stability of the Terra MODIS and Landsat 7 ETM_p sensors using pseudo-invariant test sites. *Remote Sens. Environ.* 114, 925–939.
6. INSAT-3D Data Products Format Document, 2014. Version 1.1. SAC/IMDPS/IPA/DPSG/MSDPD/TN-01/FEB 2014. (www.mosdac.gov.in/Missions/docs/INSAT3D_Products.pdf).

7. Kamei, A., et al., 2012. "Cross calibration of FORMOSAT-2 Remote Sensing Instrument (RSI) using Terra Advanced Spaceborne Thermal Emission and Reflectance Radiometer (ASTER)," *IEEE Trans. Geosci. Remote Sens.*, 50, 1–11.
8. Kerola, D. X., Bruegge, C. J., Gross, H. N., and Helmlinger, M. C., 2009. "Onorbit calibration of the EO-1 Hyperion and Advanced Land Imager (ALI) sensors using the LED Spectrometer (LSpec) automated facility," *IEEE Trans. Geosci. Remote Sens.*, 47, 1244–1255.
9. Liu, et al., C. C., 2010. "Vicarious calibration of the FORMOSAT-2 remote sensing instrument," *IEEE Trans. Geosci. Remote Sens.*, 48, 2162–2169.
10. Rao, C. R. N. (2001). Implementation of the post-launch vicarious calibration of the GOES imager visible channel (Camp Springs, MD: NOAA Satellite and Information Services (NOAA/NESDIS)). <http://www.ospo.noaa.gov/Operations/GOES/calibration/vicarious-calibration.html>.
11. Seo, S. B., 2014. "Relative compensation method for degradation of visible detectors using improved direct histogram specification," *Electron. Lett.*, 50, 446–447.
12. Teillet, P., Chander, G., 2010. Terrestrial reference standard sites for post-launch sensor calibration. *Can. J. Remote Sens.* 36, 437–450.
13. Thome, K., Schiller, K. S., Conel, J., Arai, K., & Tsuchida, S. (1998). Results of the 1997 Earth Observing System Vicarious Calibration joint campaign at Lunar Lake Playa, Nevada (USA). *Metrologia*, 35, 631–638.
14. Thome, K. J., Bigger, S. F., and Wisniewski, W., 2003. "Cross comparison of EO-1 sensors and other Earth resources sensors to Landsat-7 ETM+ using Railroad Valley Playa," *IEEE Trans. Geosci. Remote Sens.*, 41, 1180–1188.